

L-Band Radar Scattering and Soil Moisture Retrieval of Wheat, Canola and Pasture Fields for SMAP Active Algorithms

Huanting Huang¹, Tien-Hao Liao^{2, *}, Seung-Bum Kim³, Xiaolan Xu³, Leung Tsang¹, Thomas J. Jackson⁴, and Simon H. Yueh³

Abstract—Wheat, canola, and pasture are three of the major vegetation types studied during the Soil Moisture Active Passive Validation Experiment 2012 (SMAPVEX12) conducted to support NASA’s Soil Moisture Active Passive (SMAP) mission. The utilized model structure is integrated in the SMAP baseline active retrieval algorithm. Forward lookup tables (data-cubes) for VV and HH backscatters at L-band are developed for wheat and canola fields. The data-cubes have three axes: vegetation water content (VWC), root mean square (RMS) height of rough soil surface, and soil permittivity. The volume scattering and double-bounce scattering of the fields are calculated using the distorted Born approximation and the coherent reflectivity in the double-bounce scattering. The surface scattering is determined by the numerical solutions of Maxwell equations (NMM3D). The results of the data-cubes are validated with airborne radar measurements collected during SMAPVEX12 for ten wheat fields, five canola fields, and three pasture fields. The results show good agreement between the data-cube simulation and the airborne data. The root mean squared errors (RMSE) were 0.82 dB, 0.78 dB, and 1.62 dB for HH, and 0.97 dB, 1.30 dB, and 1.82 dB for VV of wheat, canola, and pasture fields, respectively. The data-cubes are next used to perform the time-series retrieval of the soil moisture. The RMSEs of the soil moisture retrieval are $0.043 \text{ cm}^3/\text{cm}^3$, $0.082 \text{ cm}^3/\text{cm}^3$, and $0.082 \text{ cm}^3/\text{cm}^3$ for wheat, canola, and pasture fields, respectively. The results of this paper expand the scope of the SMAP baseline radar algorithm for wheat, canola, and pastures formed and provide a quantitative validation of its performance. It will also have applications for the upcoming NISAR (NASA-ISRO SAR Mission).

1. INTRODUCTION

Global soil moisture measurements have many potential benefits including flood assessment, drought monitoring, global carbon balance quantification, and more. Providing this information is a goal of NASA’s Soil Moisture Active Passive (SMAP) mission [1, 2]. SMAP was launched in January 2015 utilizing an L-band radar and radiometer to provide global maps of soil moisture at 3-, 9-, and 36-km resolutions [1, 3]. However, the radar failed six months after launch on July 7, 2015. The NASA-ISRO-SAR (NISAR) mission at L-band will be launched in 2022, making possible once again the active-only as well as combined active and passive retrieval of soil moisture using L-band [4]. The NISAR mission will provide all-weather, day/night imaging of nearly the entire land and ice masses of the Earth repeated 4–6 times per month. NISAR’s orbiting radars will image at resolutions of ~ 20 meters. NISAR will also provide information on crop area over time and with enough detail to reveal changes on field scales [5]. The community identified Level 3 information product of soil moisture would benefit across

Received 7 February 2021, Accepted 6 March 2021, Scheduled 3 April 2021

* Corresponding author: Tien-Hao Liao (tien-hao.liao@jpl.caltech.edu).

¹ Radiation Laboratory, Department of Electrical Engineering and Computer Science, University of Michigan, Ann Arbor, MI 48109, USA. ² Division of Geological and Planetary Sciences, California Institute of Technology, Pasadena, CA 91125, USA. ³ Jet Propulsion Laboratory, California Institute of Technology, Pasadena, CA 91109, USA. ⁴ USDA, Agricultural Research Service, Hydrology and Remote Sensing Laboratory, Beltsville, MD 20705, USA.

agency/organization, thus increasing NISAR data utility. The product should report both the soil moisture at a specified depth and the possible addition of soil moisture anomalies. NISAR will provide maps of surface soil moisture globally every 6 to 12 days at the spatial scale of individual farm fields. This could offer unprecedented detail and is vital for monitoring the habitats of plants, animals, and humans [6, 7].

A baseline active algorithm for NISAR is being developed for the soil moisture retrieval. Empirical and semi-empirical models have been established to retrieve the soil moisture of vegetated surfaces [8–10] using backscattering coefficients, but they have limit for global retrieval because the empirical equations are derived using a small set of measurements. Complex physical scattering models have also been used to calculate the backscattering. The SMAP baseline active algorithms have been established before launch. In order to make use of the complex physical models for real time retrieval of the SMAP mission, lookup tables of backscattering were constructed. Using the measured data and lookup tables, times series retrieval of soil moisture can be carried out in real time [11, 12]. For the SMAP baseline active radar retrieval algorithm, the lookup table has the form of a data-cube with three axes: vegetation water content (VWC), root mean square (RMS) height of an isotropic surface, and soil permittivity directly related to the soil moisture [13, 14]. The SMAP baseline algorithm for radar-based retrieval inverts the data-cubes. The data-cubes were validated against the airborne and field measurements and were also used to retrieve soil moistures from the airborne radar measurements.

The SMAP active soil moisture products have been validated on a global scale including the vegetation types such as corn, soybean, pasture, and wheat (Table 1 [15]). However, at 3-km scale, vegetation types were mixed, and thorough validation of the forward model and retrieval per each crop has not been documented. The SMAP global validation did not include canola fields. Previously, the validation and soil moisture retrieval for soybean and corn vegetated surfaces were published [16, 17]. In this paper, we report on the validations and soil moisture retrievals of wheat, canola, and pastures using airborne and field measurements of SMAPVEX12. It will complete the theoretical basis of the physical models applied to SMAP’s active soil moisture algorithm. The same goal applies to the upcoming NISAR mission as it will also operate at L-band.

In vegetated surfaces, the physical models of radar backscattering at L-band are usually based on the incoherent addition from three mechanisms: volume scattering, double bounce, and surface scattering (Fig. 1). The vegetation layer is modelled with simple scatterers like cylinders and disks depending on the vegetation types, e.g., cylinders for wheat and pasture. The scatterers are embedded in the equivalent media [18] whose dielectric constant is from the Foldy’s approximation [19]. The imaginary part of the equivalent dielectric constant accounts for the attenuation homogeneously through the vegetation layer. In previous studies [20], the physical models of wheat and canola fields were derived using MIMICS (Michigan Microwave Canopy Scattering) model [21] where the first-order radiative transfer theory is used to calculate volume and double-bounce scattering. The surface scattering is computed using the physical optics model [19, 21]. In this paper, the field-based distorted Born approximation [18] derived from the averaged first order Foldy-Lax equation with the use of the T -matrix [22, 23] and half-space Green’s function is used to compute scattering from vegetation medium. The distorted Born approximation has two merits. First, double-bounce scatterings in Fig. 1(II) and (III) are exactly in phase, and thus their constructive interference known as backscattering enhancement effect has to be accounted [18, 24]. It gives a factor of 2 difference for the double-bounce term. Second, the exact Maxwell equation derived surface scattering and coherent reflectivity are applied, Maxwell equations in 3-dimensional simulations (NMM3D) [25]. The surface scattering at L-band from NMM3D simulation results is in good agreement with the experimental data whose RMS height varies from 0.55 cm to 3.47 cm [25].

The performance of the distorted Born approximation for each vegetated surface is through the validation between precomputed lookup tables, also referred as data-cubes in the paper, and the measurements from SMAPVEX12 [26]. The three axes in data-cubes are soil dielectric constant, soil RMS height, and vegetation water content (VWC). SMAPVEX12 was started at the period of early crop development and finished at the point where crops had reached maximum biomass. Since soil dielectric constant varies significantly disregarding VWC, the data-cubes provide complete coverage of its influences on backscattering coefficients. Both forward and retrieval comparisons are performed using data-cubes in this paper. Recently, hybrid methods have been developed for NMM3D simulations

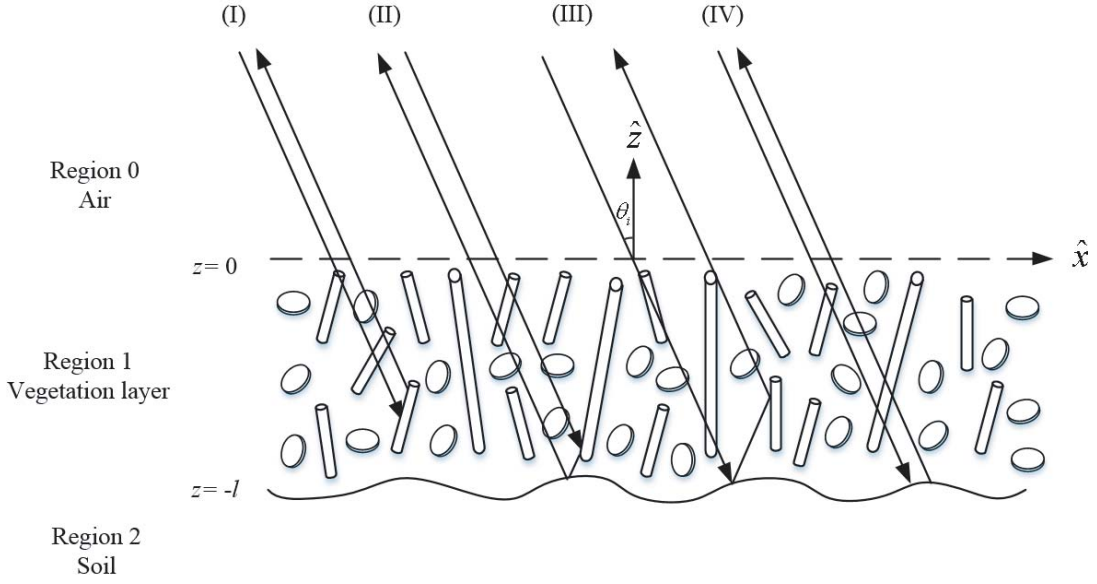


Figure 1. Backscattering of vegetated surface. The four scattering terms are: (I) volume scattering, (II) double-bounce scattering (scattering from the scatterer and then reflected by the surface), (III) double-bounce scattering (scattering of the reflected wave by a scatterer), and (IV) surface scattering.

of vegetation and forests [27–29]. The results of distorted Born approximation and data cubes in this paper are benchmark results which can be used to compare and be calibrated against NMM3D full wave simulations of vegetated media.

The outline of the paper is as follows. In Section 2, we summarize the physical model of the distorted Born approximation which together with NMM3D of rough surface forms the physical forward model for calculating the backscattering. The formulas for the three terms, volume scattering, double bounce, and surface scattering, are summarized. In Section 3, we make a comparison with the first-order radiative transfer model. In Section 4, we describe the SMAPVEX12 campaign that provides the vegetation and roughness data and airborne radar measurements. Section 5 describes the data-cubes and their evaluations. In Section 6, we apply the time-series retrieval using the data-cubes.

2. SCATTERING MODEL

In this section, we summarize the equations for the backscattering model used in this paper. We only consider the case of co-polarization backscattering rather than cross-polarization because the magnitude is larger, and the sensitivity to soil moisture is stronger. More detailed derivations are found in [30].

In the distorted Born approximation, the total backscattering σ_{pp} is the sum of the volume scattering, double bounce scattering, and surface scattering as shown in Fig. 1.

$$\sigma_{pp} = \sigma_{pp}^{vol} + \sigma_{pp}^{db} + \sigma_{pp}^{surf} \quad (1)$$

where the superscripts “vol”, “db”, and “surf” stand for “volume scattering”, “double bounce scattering”, and “surface scattering”, respectively. The subscript “pp” denotes the polarization, which is either “VV” or “HH”.

Consider an incident plane wave incident onto the medium in direction \bar{k}_i (Fig. 1).

$$\bar{k}_i = k \sin \theta_i \cos \phi_i \hat{x} + k \sin \theta_i \sin \phi_i \hat{y} - k \cos \theta_i \hat{z} \quad (2)$$

where k is the wavenumber of the microwave.

Thus, the incident direction is $(\pi - \theta_i, \phi_i)$. For spherical coordinate system, $\pi - \theta_i$ is for denoting that the incident wave is downward going. For bistatic scattering, the scattered direction is

$$\bar{k}_s = k \sin \theta_s \cos \phi_s \hat{x} + k \sin \theta_s \sin \phi_s \hat{y} + k \cos \theta_s \hat{z} \quad (3)$$

which is in the direction (θ_s, ϕ_s) .

The vegetation is assumed consisting of discrete scatterer. For a single scatterer, a far field scattering amplitude, $f_{pq}(\theta_s, \phi_s, \theta_i, \phi_i)$, which is from direction (θ_i, ϕ_i) into direction (θ_s, ϕ_s) and from polarization q into polarization p . Each scatterer scatters waves independently. The distorted Born approximation assumes that the positions of the scatterers are uniformly random. Ensemble averages denoted by angular bracket $\langle \rangle$ are also to be taken over the orientations and sizes of the scatterers. Let n_0 be the scatterers per unit volume. In the vegetation layer, the wave has an effective propagation constant (wavenumber) which is

$$k_{eff,p}(\theta, \phi) = \frac{2\pi n_0}{k} \langle f_{pp}(\theta, \phi, \theta, \phi) \rangle \quad (4)$$

This is from Foldy's approximation which is an extension of the forward scattering theorem for random media. Using phase matching, the effective propagation vector for the downward incident wave for p polarization is

$$\bar{k}_{i,eff,p} = k \sin \theta_i \cos \phi_i \hat{x} + k \sin \theta_i \sin \phi_i \hat{y} - k_{ipz} \hat{z} \quad (5)$$

where $k_{ipz} = \sqrt{k_{eff,p}^2(\pi - \theta_i, \phi_i) - k^2 \sin^2 \theta_i}$.

The effective propagation vector for the scattered wave for p polarization is

$$\bar{k}_{s,eff,p} = k \sin \theta_s \cos \phi_s \hat{x} + k \sin \theta_s \sin \phi_s \hat{y} + k_{spz} \hat{z} \quad (6)$$

where $k_{spz} = \sqrt{k_{eff,p}^2(\theta_s, \phi_s) - k^2 \sin^2 \theta_s}$.

Bistatic scattering coefficients γ_{pp}

$$\gamma_{pp}(\theta_s, \phi_s, \pi - \theta_i, \phi_i) = \frac{4\pi}{A \cos \theta_i} \langle S_{pp} S_{pp}^* \rangle \quad (7)$$

where A is the area, and S_{pp} is the bistatic scattering complex amplitude of the entire medium.

For backscattering, $\theta_s = \theta_i$; $\phi_s = \pi + \phi_i$.

1) volume scattering term is

$$\gamma_{pp}^{vol}(\theta_s, \phi_s, \pi - \theta_i, \phi_i) = \frac{4\pi n_0}{\cos \theta_i} \frac{1 - \exp(-(2\text{Im}(k_{spz}) + 2\text{Im}(k_{ipz}))d)}{(2\text{Im}(k_{spz}) + 2\text{Im}(k_{ipz}))} \langle |f_{pp}(\theta_s, \phi_s; \pi - \theta_i, \phi_i)|^2 \rangle \quad (8)$$

$f_{pp}(\theta_s, \phi_s; \pi - \theta_i, \phi_i)$ is the scattering amplitude downward propagation getting scattered upward in the vegetation.

For backscattering,

$$\sigma_{pp}^{vol} = \cos \theta_i \gamma_{pp}^{vol}(\theta_i, \pi + \phi_i, \pi - \theta_i, \phi_i) \quad (9)$$

2) There are two double bounce terms (Fig. 1): "rs" stands for first scattered downward and then reflected by the rough surface, and "sr" stands for first reflected by the rough surface followed by upward scattering by scatterer

For "rs",

$$\begin{aligned} & \gamma_{pp}^{db,rs}(\theta_s, \phi_s, \pi - \theta_i, \phi_i) \\ &= \left[\frac{4\pi n_0}{\cos \theta_i} \frac{1 - \exp(2(\text{Im}(k_{spz}) - \text{Im}(k_{ipz}))d)}{2(-\text{Im}(k_{spz}) + \text{Im}(k_{ipz}))} \right. \\ & \quad \left. \times \langle |f_{pp}(\pi - \theta_s, \phi_s; \pi - \theta_i, \phi_i)|^2 \rangle \exp(-4\text{Im}k_{spz}d) |R_p^C(\theta_s)|^2 \right] \text{ for } k_{spz} \neq (k_{ipz}) \quad (10) \end{aligned}$$

$$\begin{aligned} & \gamma_{pp}^{db,rs}(\theta_s, \phi_s, \pi - \theta_i, \phi_i) \\ &= \frac{4\pi n_0 d}{\cos \theta_i} \langle |f_{pp}(\pi - \theta_s, \phi_s; \pi - \theta_i, \phi_i)|^2 \rangle \exp(-4\text{Im}k_{spz}d) |R_p^C(\theta_s)|^2 \text{ for } k_{spz} = (k_{ipz}) \quad (11) \end{aligned}$$

where $|R_p^C(\theta_s)|^2$ is the reflectivity of the coherent wave of the rough surface at angle θ_s . The quantity is computed from NMM3D and tabulated in a lookup table.

For “*sr*”,

$$\gamma_{pp}^{db, sr}(\theta_s, \phi_s, \pi - \theta_i, \phi_i) = \left[\frac{4\pi n_0}{\cos \theta_i} \frac{1 - \exp(-2(\operatorname{Im}(k_{spz}) - \operatorname{Im}(k_{ipz}))d)}{2(\operatorname{Im}(k_{spz}) - \operatorname{Im}(k_{ipz}))} \right] \times \left\langle |f_{pp}(\theta_s, \phi_s; \theta_i, \phi_i)|^2 \right\rangle \exp(-4\operatorname{Im}k_{ipz}d) |R_p^C(\theta_i)|^2 \quad \text{for } k_{spz} \neq (k_{ipz}) \quad (12)$$

$$\gamma_{pp}^{db, sr}(\theta_s, \phi_s, \pi - \theta_i, \phi_i) = \frac{4\pi n_0 d}{\cos \theta_i} \left\langle |f_{pp}(\theta_s, \phi_s; \theta_i, \phi_i)|^2 \right\rangle \exp(-4\operatorname{Im}k_{ipz}d) |R_p^C(\theta_i)|^2 \quad \text{for } k_{spz} = (k_{ipz}) \quad (13)$$

where $|R_p^C(\theta_i)|^2$ is the reflectivity of the coherent wave of the rough surface at angle θ_i . The quantity is computed from NMM3D and tabulated in a lookup table.

For non-backscattering,

$$\gamma_{pp}^{db}(\theta_s, \phi_s, \pi - \theta_i, \phi_i) = \gamma_{pp}^{db, rs}(\theta_s, \phi_s, \pi - \theta_i, \phi_i) + \gamma_{pp}^{db, sr}(\theta_s, \phi_s, \pi - \theta_i, \phi_i) \quad (14)$$

However, in the backscattering direction, because of constructive interference, there is backscattering enhancement because

$$S_{pp}^{db, rs} = S_{pp}^{db, sr} \quad (15)$$

so that

$$S_{pp}^{db} = 2S_{pp}^{db, rs} \quad (16)$$

$$|S_{pp}^{db}|^2 = 4|S_{pp}^{db, rs}|^2 \quad (17)$$

giving a factor of 4 for the inclusion of backscattering enhancement. In this case,

$$\gamma_{pp}^{db, rs}(\theta_i, \pi + \phi_i, \pi - \theta_i, \phi_i) = \gamma_{pp}^{db, sr}(\theta_i, \pi + \phi_i, \pi - \theta_i, \phi_i) \quad (18)$$

and

$$\gamma_{pp}^{db}(\theta_i, \pi + \phi_i, \pi - \theta_i, \phi_i) = 4\gamma_{pp}^{db, rs}(\theta_i, \pi + \phi_i, \pi - \theta_i, \phi_i) \quad (19)$$

So that

$$\sigma_{pp}^{db} = 4\sigma_{pp}^{db, rs} = 4\cos \theta_i \gamma_{pp}^{db, rs}(\theta_i, \pi + \phi_i, \pi - \theta_i, \phi_i) \quad (20)$$

3) surface scattering

$$\gamma_{pp}^{sur}(\theta_s, \phi_s, \pi - \theta_i, \phi_i) = \exp(-2\operatorname{Im}(k_{spz}) + 2\operatorname{Im}(k_{ipz}))d \gamma_{pp}^{bare}(\theta_s, \phi_s, \pi - \theta_i, \phi_i) \quad (21)$$

where $\gamma_{pp}^{bare}(\theta_s, \phi_s, \pi - \theta_i, \phi_i)$ is the bistatic scattering from bare soil and is obtained from NMM3D rough surface scattering lookup table.

$$\sigma_{pp}^{sur} = \exp(-4\operatorname{Im}(k_{ipz}))d \sigma_{pp}^{bare} \quad (22)$$

3. COMPARISON WITH THE FIRST-ORDER RADIATIVE TRANSFER MODEL

In this section, we compare the formulas in the previous section with that of the first-order radiative transfer theory as used in the MIMIC model [21, 31, 32]. As physical-model based methods, both of them are well known and applied extensively. This comparison is to elaborate the similarity and difference between two methods.

The effective propagation constant is complex and consists of the real part and imaginary part

$$k_{eff,p}(\theta, \phi) = k'_{eff,p}(\theta, \phi) + ik''_{eff,p}(\theta, \phi) \quad (23)$$

The extinction rate is twice the imaginary part of the effective propagation constant accounting for two-way paths.

$$\kappa_{ep}(\theta, \phi) = 2k''_{eff,p}(\theta, \phi) \quad (24)$$

Then we have, suppressing (θ, ϕ) ,

$$k_{pz} = k'_{pz} + ik''_{pz} \quad (25)$$

We assume that the imaginary part is much less than the real part $k''_{pz} \ll k'_{pz}, k''_{eff,p} \ll k'_{eff,p}$

$$k_{pz}^2 = k_{pz}'^2 + 2ik'_{pz}k''_{pz} = k_{eff,p}^2 + 2ik'_{eff,p}k''_{eff,p} - k^2 \sin^2 \theta \quad (26)$$

Then balancing the real part and imaginary part, respectively, we obtain

$$k_{pz}'^2 = k_{eff,p}^2 - k^2 \sin^2 \theta \quad (27)$$

$$k'_{pz}k''_{pz} = k'_{eff,p}k''_{eff,p} \quad (28)$$

For most cases of wheat, grass, and canola, $k'_{eff,p}$ is very close to k , and the difference in real part is small if the vegetation layer is not too thick. Thus, we set

$$k'_{eff,p} = k \quad (29)$$

Then,

$$k'_{pz} = k \cos \theta \quad (30)$$

and

$$k''_{pz} = k''_{eff,p} \sec \theta = \frac{\kappa_{ep}}{2} \sec \theta \quad (31)$$

It is interesting to note that the real part k'_{pz} is proportional to $\cos \theta$, while the imaginary part k''_{pz} is proportional to $\sec \theta$. The $\sec \theta$ factor represents a larger attenuation due to longer path in the vegetation layer.

We further assume that

$$\kappa_{ep}(\theta_i, \pi + \phi_i) = \kappa_{ep}(\pi - \theta_i, \phi_i) \quad (32)$$

In RT theory, we use the optical depth “tau” defined by

$$\tau(\pi - \theta_i, \phi_i) = \kappa_{ep}d \quad (33)$$

The volume scattering term is

$$\sigma_{pp}^{vol}(\theta_s, \phi_s, \pi - \theta_i, \phi_i) = \cos \theta_i \frac{1 - \exp(-2\tau(\pi - \theta_i, \phi_i) \sec \theta_i)}{2\kappa_{ep}(\pi - \theta_i, \phi_i)} \left\langle 4\pi n_0 |f_{pp}(\theta_i, \pi + \phi_i; \pi - \theta_i, \phi_i)|^2 \right\rangle \quad (34)$$

The double bounce term is

$$\sigma_{pp}^{db} = 4d \exp(-2\tau(\pi - \theta_i, \phi_i) \sec \theta_i) \left\langle 4\pi n_0 |f_{pp}(\theta_i, \pi + \phi_i; \theta_i, \phi_i)|^2 \right\rangle |R_p^C(\theta_i)|^2 \quad (35)$$

The surface scattering term is

$$\sigma_{pp}^{sur} = \exp(-2\tau(\pi - \theta_i, \phi_i) \sec \theta_i) \sigma_{pp}^{bare} \quad (36)$$

The MIMIC first order RTE model is the same as above except that $\sigma_{pp}^{db}(RT)$ only has factor 2 rather than factor 4 in Equation (35) because RTE does not include backscattering enhancement. The volume scattering and surface scattering are the same. Thus, the only difference in theory between RT and DBA is a factor of 2 in the double bounce term.

4. AIRBORNE AND FIELD CAMPAIGN DATA FROM SMAPVEX12

4.1. SMAPVEX12 Campaign

As detailed in [26], SMAPVEX12 was designed to support the development and assessment of SMAP soil moisture products in an agricultural region with an area about 15 km \times 70 km located within the larger Red River Watershed south of Winnipeg, Manitoba (Canada). SMAPVEX12 was conducted between June 7 and July 19, 2012 during which soil moisture and vegetation conditions varied significantly, which provided extended-duration measurements that exceed those of any past soil moisture remote sensing field experiments. Uninhabited Aerial Vehicle Synthetic Aperture Radar (UAVSAR) [33], an aircraft-based fully polarimetric L-band radar, provided high-quality backscattering data, due to its high spatial resolution, stable platform, and reliable calibration. The aircraft carrying UAVSAR was flown several times per week, a frequency similar to that of the SMAP and NISAR satellite. Data

within the UAVSAR swath were collected over a wide range of incidence angles. These σ_0 values were normalized to an incidence angle of 40 degrees for this algorithm test in order to be applicable to the SMAP data, using the histogram-matching method [34]. The residual error in the normalization is smaller than 1 dB stdev. The speckle noise [35] was nearly removed by averaging single looks at ~ 7 m resolution over each field (~ 800 m \times 800 m). The measured backscattering coefficients are compared with the outputs from the data-cubes and also serve as the inputs for the time-series retrieval of the soil moisture, which will be illustrated in the later sections. The VWC, RMS rough surface height, and soil permittivity (soil moisture) were also measured, which are the three axes of the data-cube and inputs to sample the data-cube VV and HH. VWC was measured through destructive sampling at three sample points for each field by cutting and collecting the plants on the ground in a small area with all the measurements scaled to 1 m² area. The water content is the wet weight minus dry weight obtained by drying the sampled plants in an oven for several days, then multiplied by a conversion factor to account for the little remained water after the drying process. The RMS height of each field is assumed to be constant during SMAPVEX12 because the experiment began after seeding without further tillage operations to affect the roughness, and the effect of erosion was reduced by the vegetation canopy. The topography was approximately flat for the vegetation fields. The RMS height of the field was acquired by post-processing the data measured using the 1-m long profilometer and digital camera where repeated measurements were performed to obtain a 3-m profile consisting of three 1-m profiles for each site. During flight days, the soil moisture which changed rapidly was measured concurrently with the airborne acquisitions so that the backscatter and soil moisture data collection were near coincident. The handheld Stevens Water Hydra Probe connected to a Personal Digital Assistant was mostly used to measure the surface soil moisture with site-specific calibrations [36, 37] where individual calibration equations were developed for each of the fields. There were 16 soil moisture sample points for each field with three replicate volumetric soil moisture measurements at each point to capture spatial variability. Vegetation attributes such as crop density, plant height, stem diameter, stalk height, stalk angle, leaf thickness, and leaf width were also measured, which provided a basis for choosing the parameters for the physical forward models to compute the data-cubes. For each field, the plant density was obtained by counting the number of plants in ten rows with 1 m row length. Plant height and stem diameter were measured at the sample points for VWC just before cutting the vegetation samples with ten measurements at each point. The other vegetation attributes were measured at four wheat fields and three canola fields for five to six times during the campaign [26]. The backscattering coefficients acquired for SMAPVEX12 were normalized in the incidence angle to 40 degrees for SMAP’s focus [34]. The modelling and evaluation in this paper focus on the angle of 40-degrees only.

4.2. Vegetation and Roughness Parameters for the Wheat, Canola, and Pasture

Wheat is modeled as a layer of uniformly distributed cylinders with different orientations as shown in Fig. 2. The model parameters for the wheat data-cube presented in Table 1 are estimated from the ground measurements of SMAPVEX12. The length of the cylinders is calculated from VWC using:

$$l = \frac{VWC}{\pi a^2 \rho_{water} N_a M_{veg_{wheat}}} \tag{37}$$

where a , ρ_{water} , N_a , and M_{veg} stand for radius, water density, number of cylinders per m², and volumetric water content of vegetation, respectively. The measured length is not used because it

Table 1. Model parameters for the wheat data-cube. The probability function for scatterer elevation angle (β , measured from vertical, as shown in Fig. 2(a)) is chosen to be $p(\beta) = C \sin^2(\beta) \cos^2(\beta)$ so that a good agreement between the data-cube and measurements is achieved, where the coefficient C is determined so that the integration of $p(\beta)$ over $0 \sim 30^\circ$ is 1. The distribution of scatterer azimuth angle (α as shown in Fig. 2(a)) is uniform over all the angles.

Diameter (mm)	M_{veg}	N_a (m ⁻²)	β	α
3.6	50%	350	$0 \sim 30^\circ$	$0 \sim 360^\circ$

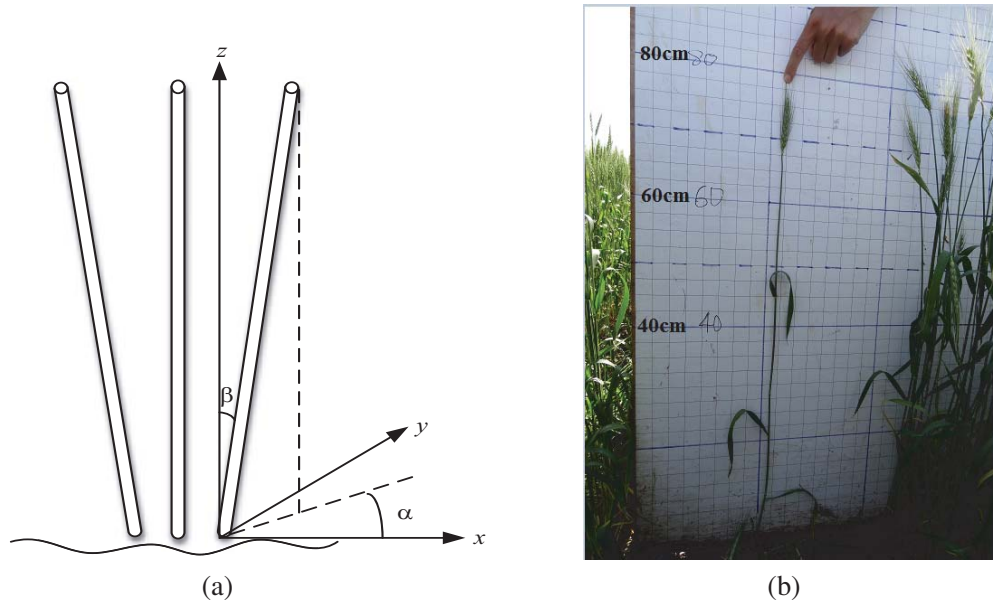


Figure 2. (a) Wheat model and pasture model. (b) Picture of wheat from the SMAPVEX12 campaign.

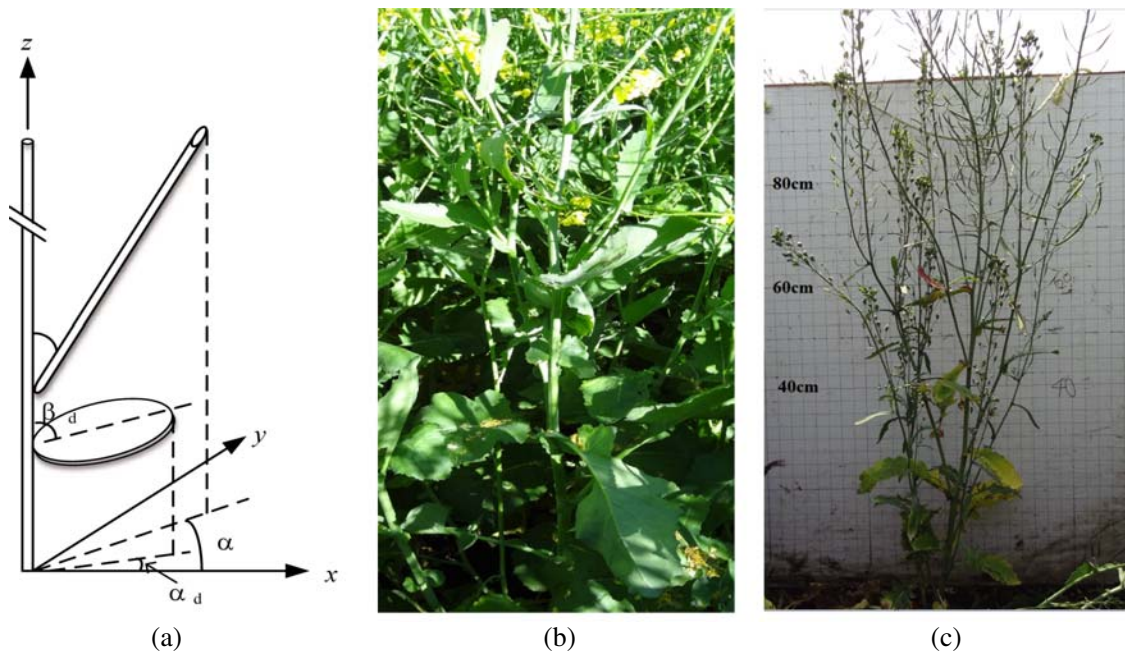


Figure 3. (a) Canola model; picture of canola from SMAPVEX12 taken at (b) June 25, (c) July 17.

was not necessarily synchronized with UAVSAR data; however, VWC was. M_{veg} is estimated from the gravimetric water content (M_g) measured during SMAPVEX12 which determines the dielectric constant [38] of a plant organ and subsequently affects the scattering by the vegetation. These parameters are used to calculate VV and HH to form the wheat data-cubes using the scattering model developed in Section 2 with different cl/s (correlation length to RMS height) ratios [16].

For canola, two different kinds of cylinders with different radii and lengths are used to model its main stem and branches while circular disks are used to model its leaves, as shown in Fig. 1 and Fig. 3(a). We use random media concept that the positions of the scatterers are random in the canola layer so

Table 2. Experimental data of SMAPVEX12 canola Field 84 at two different dates. Mv is the volumetric soil moisture, hereinafter the same.

Date	Mv	VWC	VV	HH
June 25th	0.14 cm ³ /cm ³	2.23 kg/m ²	-13.34 dB	-10.21 dB
July 17th	0.13 cm ³ /cm ³	2.37 kg/m ²	-16.95 dB	-14.74 dB

that the phase of the scattered waves are random, similar to the wheat case. Table 2 lists the measured volumetric soil moisture (Mv), VWC, VV, and HH for the same field on two different dates in June and July during SMAPVEX12. There is about a 4 dB difference for both VV and HH between those two dates even though the soil moisture as well as VWC is similar. The RMS height and cl/s ratio for the same field are approximately the same during the experiment, since they are expected to vary very little in the absence of tillage. The reason for the backscatter difference is that the leaves take larger portion of the total VWC in June than July. It can be seen from Figs. 3(b) and (c) that there were more leaves with larger radius in June than July. The backscattering of leaves increases with their radius and density. Generally, the volume scattering which is mostly contributed by the leaves dominates the total backscattering for canola (i.e., the total backscattering is mainly decided by the scattering of leaves.) Thus, for the two cases with the same VWC, the sum of VWC from leaves, branches, and main stems, the one with more leaves generates more backscattering.

In the data-cubes, each set of input (Mv, VWC, RMS height, and cl/s ratio) should produce only one unique set of VV and HH. Thus, two different data-cubes computed from different model parameters are needed for canola in order to account for the two significantly different VV and HH values in Table 2. In the evaluation of the data-cube and its inversion for soil moisture retrieval, it will be necessary to know when to use the appropriate data-cube. As shown in Fig. 4, there was a large decrease in the measured (VV + HH)/2 between July 8th and July 10th for all the canola fields despite the fact that there was no significant decrease in soil moisture or VWC based upon the ground measurement data in Table 3. Therefore, a switch is made in the data-cube used beginning July 10th (July data-cube). It is also noticed in Fig. 4 that the (VV + HH)/2 for canola Field 115 was much smaller than that of the other fields in June, so the July data-cube, which produced smaller VV and HH, was used for Field 115 over the entire period. The parameters used to generate the two data-cubes are listed in Table 4. M_{veg} and leaf radius are adjusted to smaller values for the July data-cube based on the ground measurement data, which can also be seen from Figs. 3(b) and (c) that the canola in July appears withered compared to

Table 3. Change of Mv and VWC for the canola fields (July 10th minus July 8th).

Field No.	61	84	115	122	124
ΔMv (cm ³ /cm ³)	0.056	0.084	-0.064	0.0048	0.029
ΔVWC (kg/m ²)	0.10	0.10	0.074	-0.20	-0.38

Table 4. Model parameters for the canola data-cubes. The M_{veg} values in plain font and in parentheses are used for June and July data-cube, respectively. M_{veg} is estimated from the measured M_g in the way as the wheat [38]. VWC is measured in situ. d and l are derived from VWC based on the empirical allometry relationships. The distribution of azimuthal angle (α as shown in Fig. 3(a)) is uniform over $0 \sim 360^\circ$ for the stem, branch and leaf.

	Diameter (mm)	Length (cm)	M_{veg}	Distribution of β
Stem	d	l	60% (40%)	Uniform over $0 \sim 5^\circ$
Branch	$d/2$	$l/3$	60% (40%)	Uniform over $0 \sim 35^\circ$
Leaf	140 (80)	0.03	60% (40%)	Uniform over $40^\circ \sim 90^\circ$

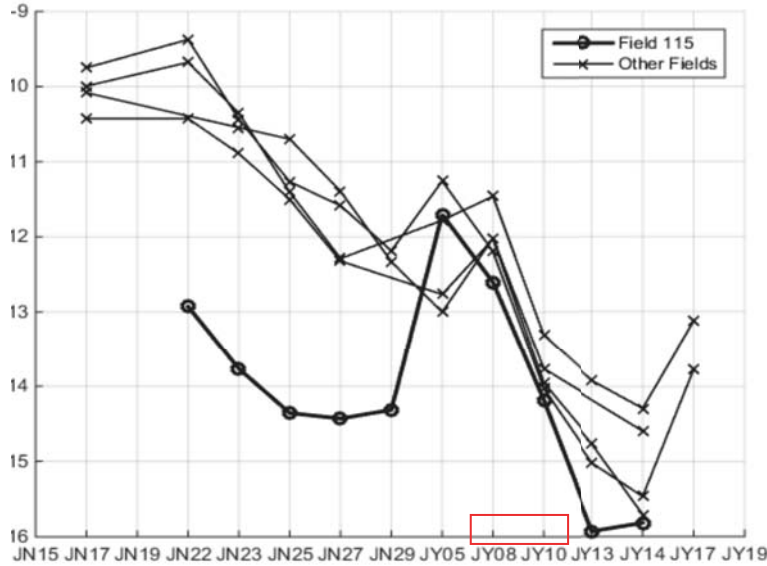


Figure 4. $(VV + HH)/2$ measurement data for the five SMAPVEX12 canola fields: large decrease observed between July 8th and 10th. The x -axis presents time: “JN” stands for “June” while “JY” stands for “July”, hereinafter the same.

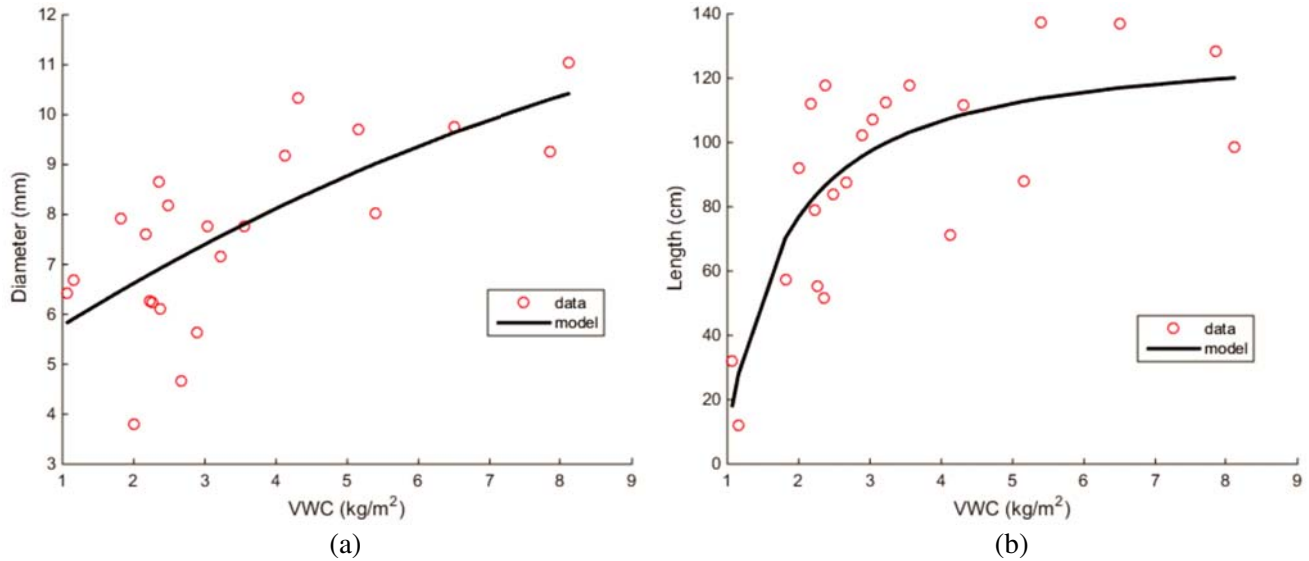


Figure 5. Vegetation parameters during SMAPVEX12: (a) Main stem diameter as a function of VWC; (b) Main stem length as a function of VWC.

conditions in June. From the in situ measurements, the average number of canola plants per m^2 (N_a) is about 60, and the number of leaves per plant (N_l) is about b ($b = 2$ and 1 for June and July data-cubes, respectively.) times the number of branches per plant (N_s). The main stem diameter (d) which increases with VWC is calculated from the allometric relationship with VWC obtained from the measurement data through curve fitting: $d_{fit} = -0.03135VWC^2 + 0.938VWC + 4.87$ in mm, as shown in Fig. 5(a). d is adjusted to be $2/3$ of the curve fitting value (i.e., $d = d_{fit}/1.5$) to best fit the data. Similarly, the main stem length (l) is obtained as: $l = -121.4VWC^{-1.186} + 130.2$ in cm, shown in Fig. 5(b). N_s can

Table 5. Model parameters for the pasture data-cube. The probability function for scatterer elevation angle (β , measured from vertical, as shown in Fig. 2(a)) is chosen to be $p(\beta) = C \sin^2(\beta) \cos^0(\beta)$ so that a good agreement between the data-cube and measurements is achieved, where the coefficient C is determined so that the integration of $p(\beta)$ over $0^\circ \sim 90^\circ$ is 1. The distribution of scatterer azimuth angle (α as shown in Fig. 2(a)) is uniform over all the angles.

Diameter (mm)	M_{veg}	Length (cm)	β	α
2	60%	20	$0^\circ \sim 90^\circ$	$0 \sim 360^\circ$

be calculated from WVC using the following formula:

$$N_s = \frac{WVC - \rho_{water} N_a Vol_{stem} M_{veg_{stem}}}{N_a \rho_{water} (Vol_{branch} M_{veg_{branch}} + b Vol_{leaf} M_{veg_{leaf}})} \tag{38}$$

where Vol_{stem} , Vol_{branch} and Vol_{leaf} are the volume of stem, branch, and leaf, respectively.

Pasture is also modeled as a layer of uniformly distributed cylinders. However, the dependence of vegetation parameters against WVC is through density. The parameters are listed in Table 5. The dependence is relatively simple compared to canola and wheat. The data-cube is generated based on M_v , WVC, and RMS height. For the surface roughness, we fix the correlation length to RMS height ratio to be 10.

$$N_a = \frac{WVC}{\rho_{water} \pi a^2 l M_{veg_{pasture}}} \tag{39}$$

5. EVALUATION OF THE WHEAT, CANOLA, AND PASTURE DATA-CUBES

First, we compute the data-cubes using the model described in Section 2 and using vegetation and roughness parameters as measured in Section 3.

A data-cube is a lookup table with the three axes representing three inputs: (1) real part of soil permittivity ($\epsilon_{psr_{soil}}$), (2) RMS height, (3) WVC, and the outputs are VV and HH, where $\epsilon_{psr_{soil}}$ is directly related to soil moisture [12, 13]. The axis ranges of the data-cube are 0.1 cm \sim 4.0 cm for RMS height and 3 \sim 30 for real part of $\epsilon_{psr_{soil}}$. The range for WVC depends on the typical WVC values for the crop. The wheat data-cube is plotted in Fig. 6.

The data-cubes are evaluated by comparing with the backscatter measurements from the UAVSAR for the ten wheat fields, five canola fields, and three pasture fields studied during SMAPVEX12. The

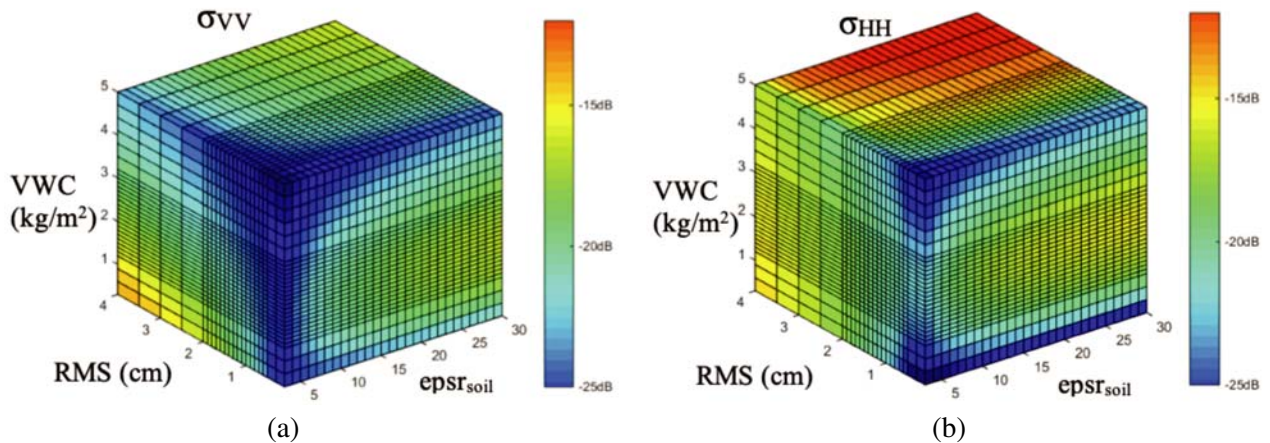


Figure 6. Wheat data-cube, (a) σ_{VV} , (b) σ_{HH} . Three axes are: (1) Vegetation Water Content (WVC) in kg/m^2 , (2) RMS height of bare soil in cm at frequency 1.26 GHz, (3) $\epsilon_{psr_{soil}}$, from which corresponding soil moisture can be obtained via the dielectric model for soil [13]).

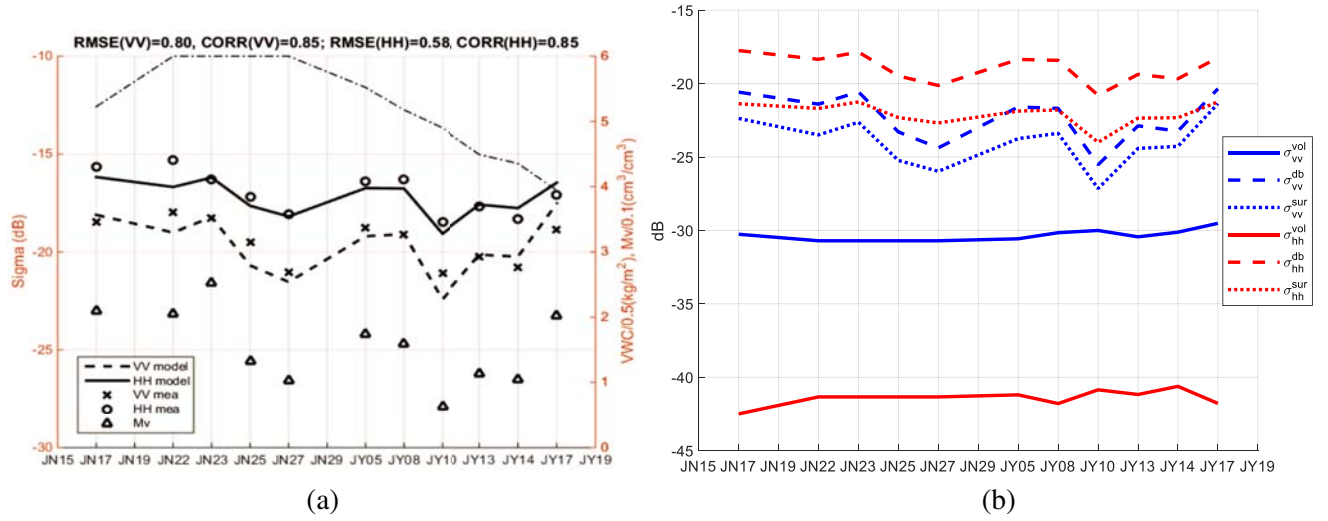


Figure 7. Wheat data-cube applied to SMAPVEX12 wheat Field 91 with $cl/s = 15$. (a) ‘CORR’ is short for ‘correlation coefficient’. The dash-dot curve plots VWC, hereinafter the same. ‘VV model’ and ‘HH model’ indicate the backscatters from the data-cube. ‘VV mea’ and ‘HH mea’ represent the measured backscatters from the UAVSAR. Soil moisture (Mv) and VWC are scaled as $Mv/0.1$ and $VWC/0.5$ for plot, respectively. (b) Breakdown of the contributions of each of the three terms of volume scattering, double bounce and surface scattering.

measured RMS height, VWC, and in situ soil moisture are used as inputs to the data-cube to estimate VV and HH that are then compared to the UAVSAR data for each day of flight. An example of the time-series forward comparison between the data-cube and the UAVSAR data for one of the wheat fields is presented in Fig. 7(a), which has the RMSE, defined in Equation (40), of 0.80 dB and 0.58 dB for VV and HH, respectively. Fig. 7(b) and Table 6 presents the detail breakdown of the three scattering terms: volume scattering, double bounce and surface scattering. It is observed that, for wheat fields, the double bounce and surface scattering generally dominates, while the volume scattering is very small.

Table 6. Detailed breakdown of the three scattering terms: volume scattering, double bounce and surface scattering for wheat field 91. The unit for the scattering coefficient is dB. The coherent reflectivity ($|R_v^C|^2$ and $|R_h^C|^2$) and optical thickness (τ_v and τ_h) are unitless.

Date	6/17	6/22	6/23	6/25	6/27	7/5	7/8	7/10	7/13	7/14	7/17
σ_{vv}	-18.10	-19.01	-18.21	-20.69	-21.53	-19.20	-19.09	-22.42	-20.14	-20.24	-17.54
σ_{vv}^{vol}	-30.26	-30.71	-30.71	-30.71	-30.71	-30.57	-30.16	-30.00	-30.44	-30.12	-29.52
σ_{vv}^{db}	-20.58	-21.40	-20.57	-23.29	-24.38	-21.59	-21.69	-25.53	-22.88	-23.23	-20.35
σ_{vv}^{sur}	-22.37	-23.49	-22.63	-25.24	-25.97	-23.74	-23.39	-27.15	-24.41	-24.27	-21.37
$ R_v^C ^2$	0.18	0.17	0.21	0.11	0.10	0.14	0.14	0.06	0.10	0.10	0.17
τ_v	0.48	0.55	0.55	0.55	0.55	0.50	0.47	0.45	0.41	0.40	0.36
σ_{hh}	-16.17	-16.68	-16.20	-17.64	-18.19	-16.74	-16.76	-19.07	-17.58	-17.76	-16.46
σ_{hh}^{vol}	-42.50	-41.34	-41.34	-41.34	-41.34	-41.20	-41.79	-40.86	-41.18	-40.62	-41.78
σ_{hh}^{db}	-17.75	-18.35	-17.85	-19.48	-20.13	-18.35	-18.42	-20.79	-19.37	-19.67	-18.24
σ_{hh}^{sur}	-21.37	-21.69	-21.25	-22.32	-22.68	-21.87	-21.80	-24.00	-22.35	-22.32	-21.25
$ R_h^C ^2$	0.36	0.34	0.38	0.27	0.25	0.31	0.31	0.18	0.25	0.25	0.34
τ_h	0.10	0.12	0.12	0.12	0.12	0.11	0.10	0.09	0.09	0.08	0.08

Both double bounce and surface scattering increase with soil moisture. This makes the backscattering coefficients from the wheat fields generally have a positive correlation with the soil moisture.

$$RMSE = \sqrt{\frac{1}{N} \sum_{i=1}^N (\sigma_{data,i} - \sigma_{cube,i})^2} \quad (40)$$

where N is the number of samples, σ_{data} the measured backscattering coefficient, and σ_{cube} the predicted backscattering coefficient from the data-cube.

Similarly, Fig. 8 is one example for the canola fields (RMSE values of 0.66 dB and 0.60 dB and correlation coefficients of 0.95 and 0.98 for VV and HH, respectively). From Fig. 8(b) and Table 7, it is observed that the volume scattering and double bounce generally dominate among the three scattering terms for canola fields.

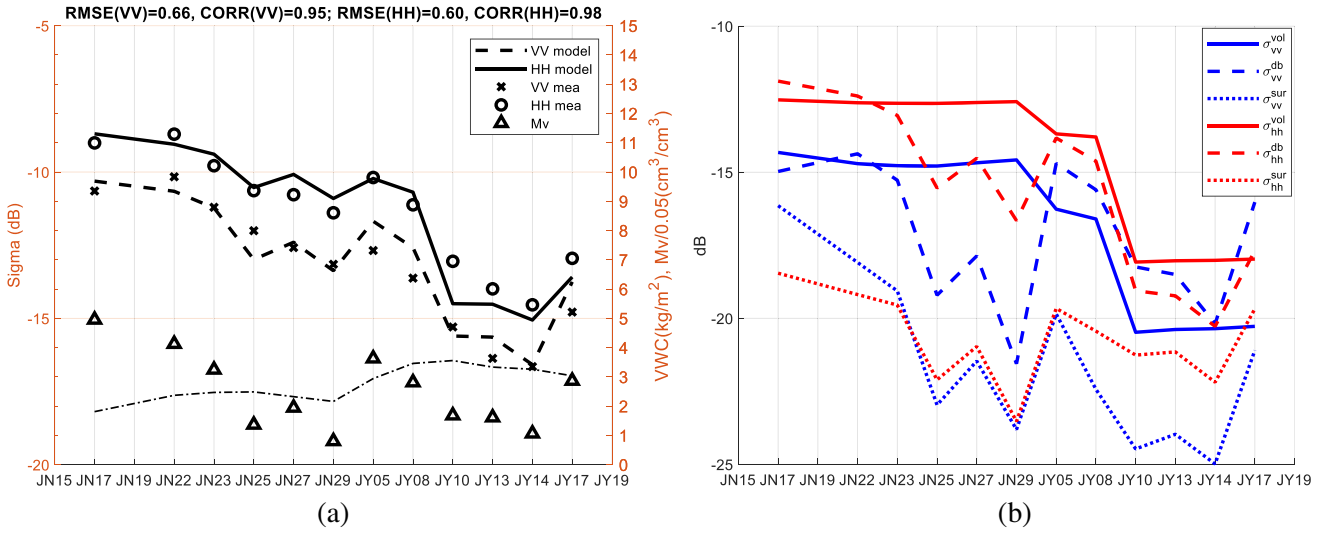


Figure 8. Canola data-cubes applied to SMAPVEX12 canola Field 61 with $cl/s = 4$. (a) Soil moisture (Mv) is scaled as $Mv/0.05$ for plot. (b) Breakdown of the contributions of each of the three terms of volume scattering, double bounce and surface scattering.

Fig. 9 is the forward model comparison for pasture field 21 (RMSE values of 0.54 dB and 0.75 dB and correlation coefficients of 0.58 and 0.55 for VV and HH, respectively). From the breakdown of scattering mechanisms in Fig. 9(b) and Table 8, surface scattering dominates VV, and double bounce dominates HH.

The forward comparisons for all the wheat, canola, and pasture fields are presented using the scatter plots in Fig. 10, Fig. 11, and Fig. 12. The RMSE and correlation coefficient for each field are listed in Table 9, Table 10, and Table 11. The RMSEs for all the wheat fields are 0.97 dB for VV and 0.82 dB for HH while the RMSEs for all the canola fields are 1.30 dB for VV and 0.78 dB for HH. The RMSEs for all the pasture fields are 1.82 dB for VV and 1.62 dB for HH. The systematic error (E_{sys}), residual error (E_{res}), and total error (E_{tot}) defined as below [20] are also calculated for all the wheat and canola fields.

$$E_{sys} = \frac{1}{N} \sum_{i=1}^N (\sigma_{data,i} - \sigma_{cube,i}) \quad (41)$$

$$E_{res} = \sqrt{\frac{1}{N} \sum_{i=1}^N (|\sigma_{data,i} - \sigma_{cube,i}| - |E_{sys}|)^2} \quad (42)$$

$$E_{tot} = \sqrt{E_{sys}^2 + E_{res}^2} \quad (43)$$

Table 7. Detailed breakdown of the three scattering terms: volume scattering, double bounce and surface scattering for canola field 61. The unit for the scattering coefficient is dB. The coherent reflectivity ($|R_v^C|^2$ and $|R_h^C|^2$) and optical thickness (τ_v and τ_h) are unitless.

Date	6/17	6/22	6/23	6/25	6/27	6/29	7/5	7/8	7/10	7/13	7/14	7/17
σ_{vv}	-10.31	-10.66	-11.23	-12.99	-12.40	-13.37	-11.68	-12.59	-15.60	-15.64	-16.58	-13.75
σ_{vv}^{vol}	-14.32	-14.71	-14.77	-14.79	-14.68	-14.58	-16.26	-16.60	-20.48	-20.38	-20.35	-20.28
σ_{vv}^{db}	-14.97	-14.37	-15.27	-19.21	-17.86	-21.55	-14.70	-15.60	-18.24	-18.50	-20.19	-16.02
σ_{vv}^{sur}	-16.14	-18.09	-19.06	-22.97	-21.46	-23.81	-19.85	-22.43	-24.47	-23.97	-24.99	-21.10
$ R_v^C ^2$	0.17	0.14	0.12	0.05	0.07	0.03	0.13	0.10	0.07	0.07	0.05	0.11
τ_v	0.27	0.37	0.38	0.39	0.36	0.33	0.49	0.59	0.62	0.58	0.56	0.52
σ_{hh}	-8.69	-9.05	-9.39	-10.53	-10.08	-10.90	-10.22	-10.69	-14.50	-14.52	-15.06	-13.59
σ_{hh}^{vol}	-12.52	-12.62	-12.64	-12.64	-12.61	-12.58	-13.69	-13.79	-18.07	-18.03	-18.02	-17.97
σ_{hh}^{db}	-11.88	-12.39	-13.06	-15.54	-14.52	-16.65	-13.83	-14.62	-19.06	-19.23	-20.28	-17.68
σ_{hh}^{sur}	-18.46	-19.19	-19.55	-22.11	-20.96	-23.53	-19.66	-20.44	-21.26	-21.15	-22.19	-19.67
$ R_h^C ^2$	0.35	0.31	0.28	0.16	0.19	0.11	0.30	0.24	0.19	0.19	0.16	0.26
τ_h	0.19	0.21	0.21	0.21	0.20	0.20	0.23	0.26	0.23	0.22	0.22	0.21

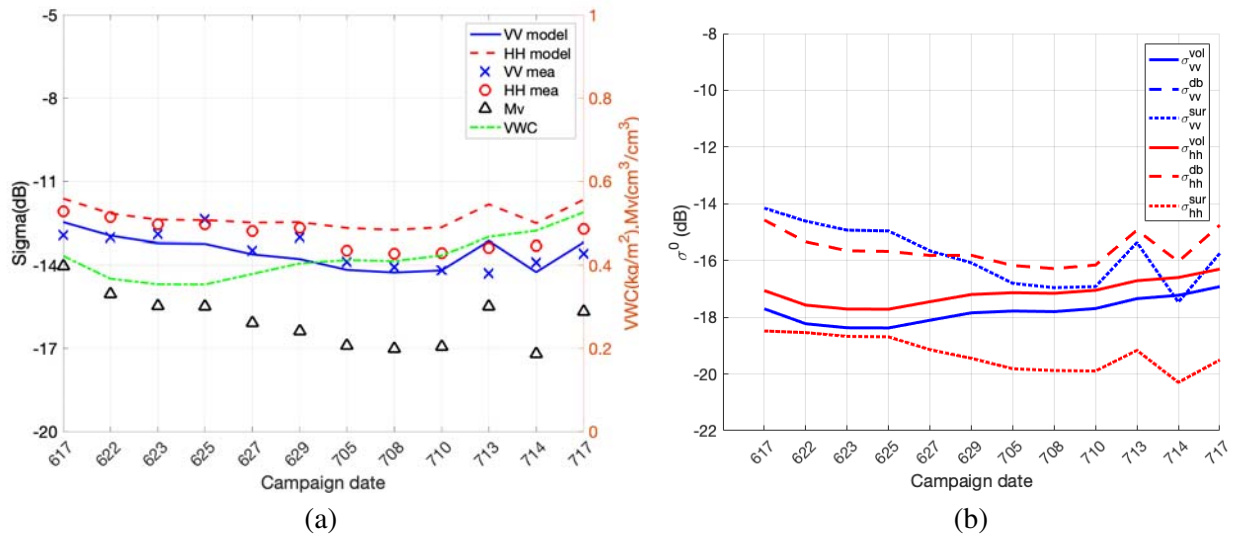


Figure 9. Data-cubes applied to SMAPVEX12 pasture Field 21 with $cl/s = 10$. (a) Forward model comparison against measured backscatters. (b) Breakdown of the contributions of each of the three terms of volume scattering, double bounce and surface scattering.

The results are compared with [20] at 40 degrees incident angle and L-band as shown in Table 12 and Table 13 for wheat and canola, respectively. In terms of the number of fields, SMAPVEX12 with ten wheat fields and five canola fields provides more extensive measurement data than [20] which has two wheat fields and two canola fields. The total error from the wheat data-cube is smaller than that from [20], especially compared to the VV of site #12 where the total error from the data-cube is 0.64 dB less. For the canola data-cubes, the total error is also smaller than that from [20] and is 1.42 dB smaller than site #23 for VV.

Some sources of error to be considered when interpreting the results are: (1) the ground measurements of RMS height, VWC, and soil moisture (e.g., the RMS height was likely to be influenced by the rain which would flatten the soil surface, but a constant RMS height was used during the whole

Table 8. Detailed breakdown of the three scattering terms: volume scattering, double bounce and surface scattering for pasture field 21. The unit for the scattering coefficient is dB. The coherent reflectivity ($|R_v^C|^2$ and $|R_h^C|^2$) and optical thickness (τ_v and τ_h) are unitless.

Date	6/17	6/22	6/23	6/25	6/27	6/29	7/5	7/8	7/10	7/13	7/14	7/17
σ_{vv}	-12.47	-12.95	-13.22	-13.24	-13.61	-13.78	-14.17	-14.27	-14.19	-13.13	-14.25	-13.18
σ_{vv}^{vol}	-17.70	-18.23	-18.37	-18.38	-18.11	-17.85	-17.78	-17.80	-17.69	-17.34	-17.23	-16.92
σ_{vv}^{db}	-29.35	-30.42	-30.88	-30.92	-31.27	-31.38	-32.01	-32.19	-32.02	-30.10	-32.00	-29.95
σ_{vv}^{sur}	-14.15	-14.61	-14.93	-14.96	-15.66	-16.08	-16.81	-16.96	-16.92	-15.37	-17.47	-15.75
$ R_v^C ^2$	0.26	0.23	0.21	0.21	0.18	0.17	0.15	0.14	0.14	0.21	0.13	0.2
τ_v	0.14	0.12	0.11	0.11	0.12	0.13	0.13	0.13	0.13	0.15	0.16	0.17
σ_{hh}	-11.62	-12.16	-12.38	-12.39	-12.48	-12.47	-12.68	-12.75	-12.65	-11.83	-12.50	-11.66
σ_{hh}^{vol}	-17.06	-17.57	-17.71	-17.72	-17.45	-17.20	-17.14	-17.16	-17.05	-16.71	-16.60	-16.30
σ_{hh}^{db}	-14.57	-15.34	-15.66	-15.68	-15.82	-15.82	-16.18	-16.28	-16.16	-14.93	-16.04	-14.75
σ_{hh}^{sur}	-18.48	-18.54	-18.68	-18.69	-19.14	-19.45	-19.82	-19.88	-19.90	-19.17	-20.30	-19.51
$ R_h^C ^2$	0.43	0.39	0.38	0.37	0.35	0.33	0.3	0.3	0.3	0.37	0.29	0.37
τ_h	0.16	0.14	0.13	0.13	0.14	0.15	0.15	0.15	0.15	0.17	0.18	0.2

Table 9. RMSE and correlation coefficient of backscatters between data-cube simulations and UAVSAR observations for the ten wheat fields.

Field No.	RMSE (dB)		Correlation Coefficient	
	VV	HH	VV	HH
91	0.80	0.58	0.85	0.85
85	0.91	0.87	0.62	0.87
81	1.37	0.84	0.88	0.94
74	0.66	0.98	0.88	0.91
73	0.56	1.03	0.99	0.92
65	1.51	0.64	0.95	0.96
44	1.04	0.87	0.83	0.89
42	1.04	0.74	0.82	0.89
41	0.62	0.56	0.90	0.98
31	1.02	0.91	0.82	0.97

Table 10. RMSE and correlation coefficient of backscatters between data-cube simulations and UAVSAR observations for the five canola fields.

Field No.	RMSE (dB)		Correlation Coefficient	
	VV	HH	VV	HH
124	1.75	0.47	0.45	0.95
122	0.94	0.60	0.87	0.96
115	1.46	1.23	0.79	0.57
84	1.55	0.78	0.86	0.95
61	0.66	0.60	0.95	0.98

Table 11. RMSE and correlation coefficient of backscatters between data-cube simulations and UAVSAR observations for the three pasture fields.

Field No.	RMSE (dB)		Correlation Coefficient	
	VV	HH	VV	HH
21	0.54	0.75	0.58	0.55
22	2.22	2.11	0.64	0.33
23	2.28	1.77	0.81	-0.23

study period for each field.); (2) UAVSAR data (e.g., there is normalization error when normalizing the raw data to 40° , and the RMSE is about 1 dB. [26].); (3) Data-cube parameters (e.g., the plant density is generally different for different fields, and only an average value is used in the data-cube that is applied

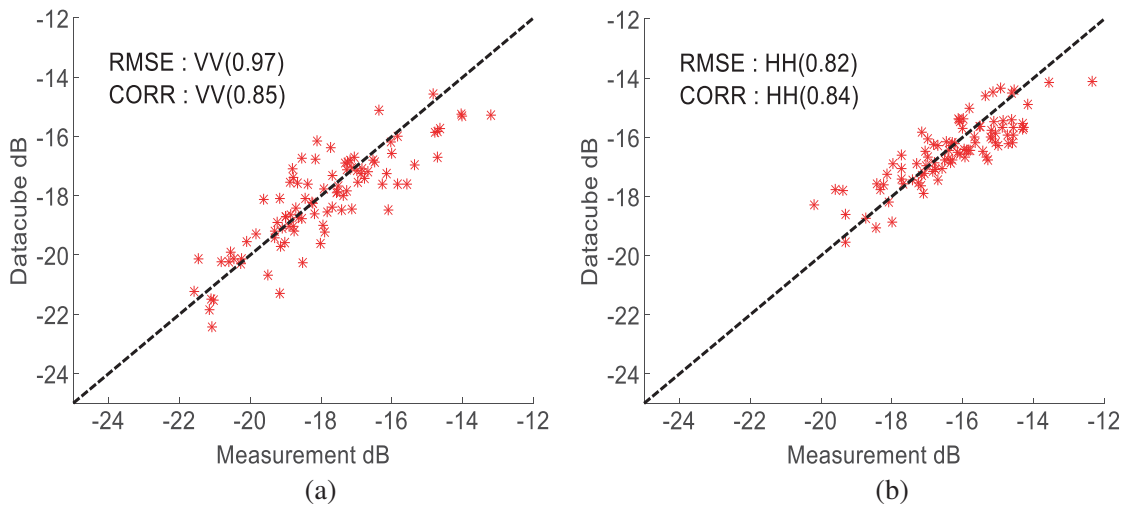


Figure 10. Comparison between the data-cube and UAVSAR measurements for the ten SMAPVEX12 wheat fields (a) VV, (b) HH.

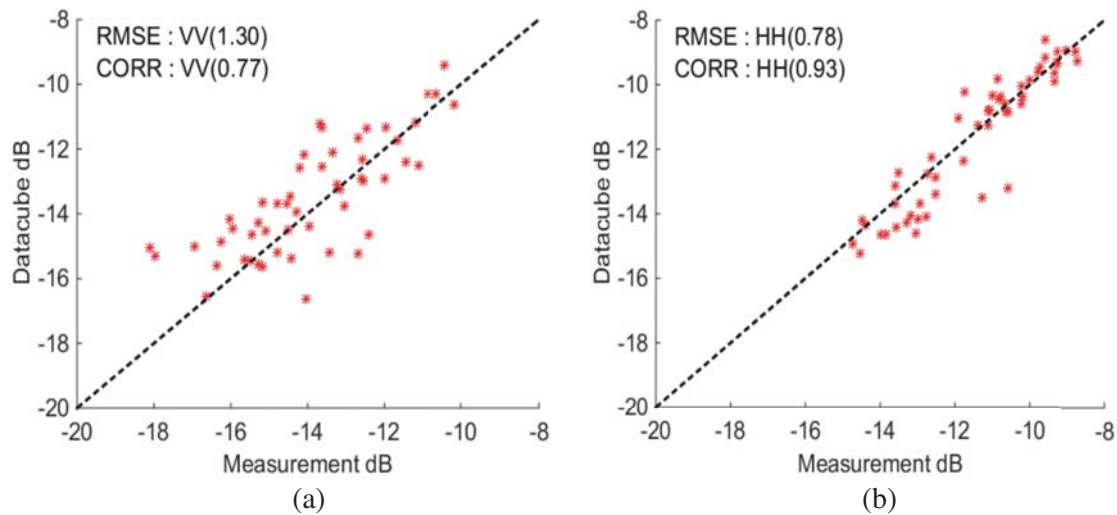


Figure 11. Comparison between the data-cube and UAVSAR measurements for the five SMAPVEX12 canola fields (a) VV, (b) HH.

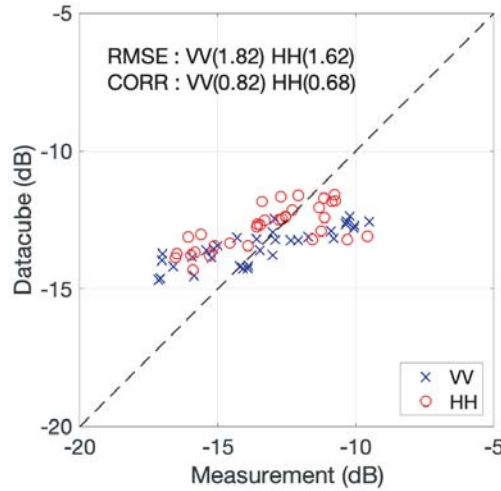


Figure 12. Add comparison between the data-cube and UAVSAR measurements for the three SMAPVEX12 pasture fields, VV & HH.

Table 12. Error of estimated backscatters for wheat, compared with [20].

	E_{sys} (dB)		E_{res} (dB)		E_{tot} (dB)	
	VV	HH	VV	HH	VV	HH
Site #12 of [20]	-1.17	-0.10	0.91	0.68	1.48	0.96
Site #13 of [20]	-0.57	0.63	0.76	0.47	0.95	0.79
Ten SMAPVEX12 Fields	0.20	0.17	0.82	0.68	0.84	0.70

Table 13. Error of estimated backscatters for canola, compared with [20].

	E_{sys} (dB)		E_{res} (dB)		E_{tot} (dB)	
	VV	HH	VV	HH	VV	HH
Site #23 of [20]	-2.27	-0.51	1.06	0.70	2.51	0.86
Site #31 of [20]	-0.18	0.18	1.08	0.73	1.09	0.75
Five SMAPVEX12 Fields	-0.34	0.18	1.03	0.66	1.08	0.69

to all the fields.); (4) Scattering model (e.g., the scatterers are assumed to be uniformly distributed in the vegetation layer which is hard to be true for the crop fields. Also, the space between rows is not taken into account where the surface scattering is larger than that from the current model because of no attenuation by the vegetation layer.)

The results of Fig. 10, Fig. 11, and Fig. 12 show that the data-cube model predictions are in good agreement with airborne radar measurements.

6. DATA-CUBE BASED SOIL MOISTURE RETRIEVAL

The data-cubes developed above are used here to retrieve the soil moisture. Based on the time-series retrieval algorithm developed for the SMAP mission [12], the measured VV and HH of all the N days collected in a specific field are the inputs. The outputs are N values of VWC and epsr_{soil} as well as the RMS height. epsr_{soil} is then converted to soil moisture using the Mironov dielectric model [13] with the ancillary data on the clay fraction of the soil. It is assumed that the RMS height remains

unchanged over the retrieval period. The retrieval approach then minimizes the difference between the measurement and the data-cube over all the N days as defined in the cost function below where w_{VV} and w_{HH} are the weighting factors which are uniform in time and also the same for VV and HH in the case of SMAP radar [11].

$$\text{cost} = \sum_{\text{day}=1}^N \left[w_{VV} (VV_{\text{data}} - VV_{\text{cube}})^2 + w_{HH} (HH_{\text{data}} - HH_{\text{cube}})^2 \right] \quad (44)$$

The number of unknowns ($2N + 1$) is larger than that of inputs ($2N$), so some constraints should be added during the retrieval to avoid the improper solutions. In this paper, a VWC constraint is used under the assumption that the vegetation will not change significantly during an observation cycle. The ratio of the VWC between two sequential observation days (larger one divided by the smaller one) is assumed to be less than 1.10 and 1.14 for wheat and canola, respectively, according to the measured VWC of all the fields as shown in Fig. 13 and Fig. 14.

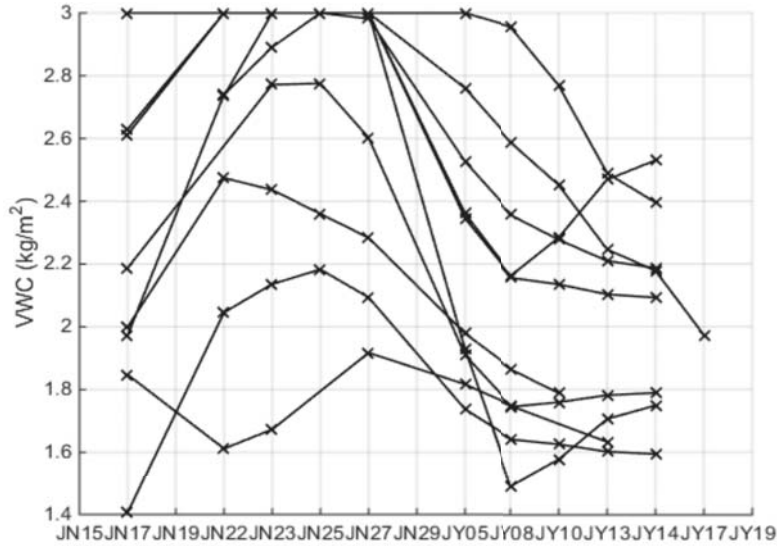


Figure 13. VWC of the ten SMAPVEX12 wheat fields.

The wheat data-cube is applied to the soil moisture retrieval of the ten wheat fields. Fig. 15 shows one example for the time-series retrieval of wheat Field 91 where the RMSE is $0.026 \text{ cm}^3/\text{cm}^3$ with correlation coefficient of 0.91. The retrieval results for all the ten wheat fields are presented in Fig. 16. The RMSE and correlation coefficient values for each field are listed in Table 14. The correlation coefficient is 0.94, and the RMSE is $0.043 \text{ cm}^3/\text{cm}^3$ which is about the same as that obtained for bare soil [11] despite the fact that there were substantial levels of vegetation effect during SMAPVEX12. The RMSE is better than that for the pasture fields [12] (the vegetation structure is similar between pasture and wheat although the scatterer orientation angle may differ.)

As described earlier, there are two data-cubes for canola, so it is important to decide which data-cube to use during the soil moisture retrieval. The approach based upon the campaign date used in the forward comparison is not suitable for retrieval because the satellite mission (e.g., NISAR) is for global soil moisture retrieval, and the canola growth stage could vary at the same time in different areas. Based on Fig. 4 where $(VV + HH)/2$ became less than -13 dB since July 10th, thus when $(VV + HH)/2$ is less than -13 dB , the July data-cube should be used; otherwise, the other data-cube should be used. Similarly, the retrieval results are presented in Fig. 17, Fig. 18, and Table 15 with the averaged RMSE of $0.082 \text{ cm}^3/\text{cm}^3$ for all the five canola fields. As presented in Section 5, the averaged RMSE of the backscattering coefficients between the data-cube and the measurement for all the fields in the forward comparison is similar for the wheat and canola which is around 1 dB. However, the soil moisture retrieval results for wheat are much better than those for canola. The main reason is that the backscattering

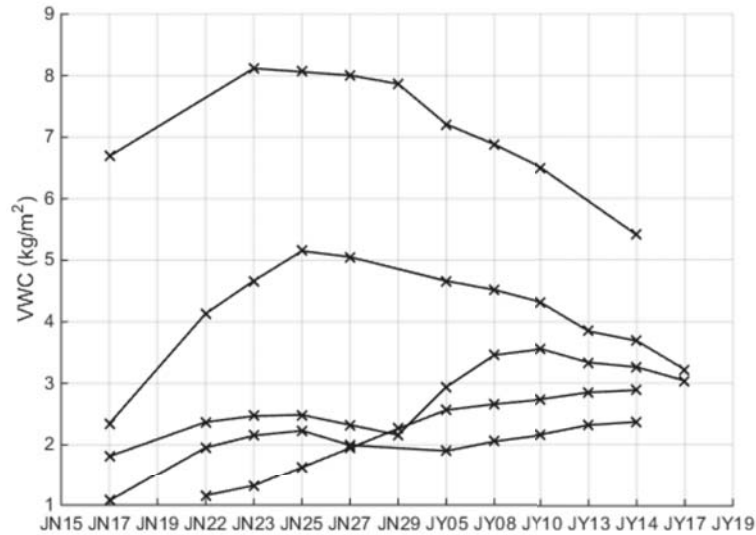


Figure 14. VWC of the five SMAPVEX12 canola fields (The scale of the y axis is different from that of Fig. 11).

Table 14. RMSE and correlation coefficient of soil moisture between retrieval results and ground measurements for the ten wheat fields.

Field No.	RMSE (cm^3/cm^3)	Correlation Coefficient
91	0.026	0.91
85	0.034	0.89
81	0.025	0.91
74	0.034	0.99
73	0.053	0.97
65	0.042	0.96
44	0.056	0.88
42	0.051	0.92
41	0.032	0.96
31	0.061	0.94

coefficient of wheat is more sensitive to the soil moisture than that of canola, especially for VV. This is because the double-bounce and surface scattering, which depend significantly on the soil permittivity, usually dominate among the three backscattering mechanisms for wheat. On the other hand, volume scattering, which is independent of the soil moisture and only depends on the VWC, usually dominates for canola while the soil surface scattering is relatively small because of the significant attenuation from the generally large VWC as shown in Fig. 14. Another reason for the retrieval error of canola is its large VWC range ($1 \text{ kg/m}^2 \sim 9 \text{ kg/m}^2$) and the uncertainties associated with estimating it over this large range.

The pasture data-cube is applied to the soil moisture retrieval of the ten wheat fields. Fig. 19 shows the time-series retrieval of pasture field 21 where the RMSE is $0.06 \text{ cm}^3/\text{cm}^3$ with correlation coefficient of 0.54. The retrieved results for all the three pasture fields are presented in Fig. 20. The RMSE and correlation coefficient values for each field are listed in Table 16. Note that the cost function for pasture field is optimized by choosing $w_{VV} = 0.9$ and $w_{HH} = 0.1$. This causes VV data-cube more dominating in the overall retrieval performance.

The data-cubes are applicable to the retrieval over the wheat and canola land cover classes, since

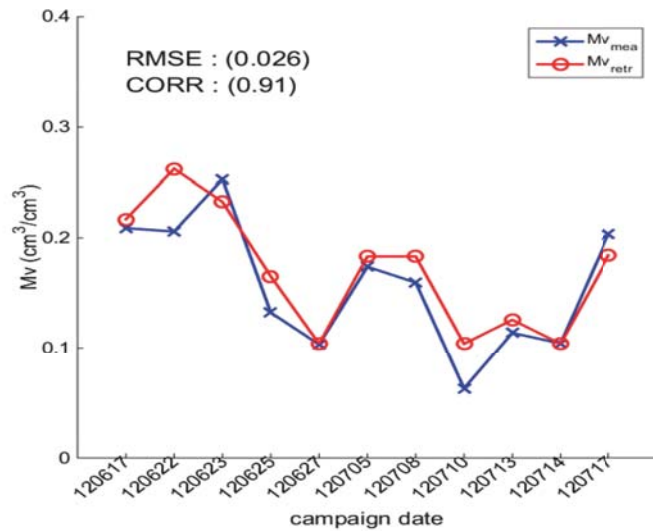


Figure 15. Time-series soil moisture retrieval for SMAPVEX12 wheat Field 91. Mv_{mea} stands for the measured soil moisture while Mv_{retr} stands for the data-cube retrieved soil moisture, hereinafter the same.

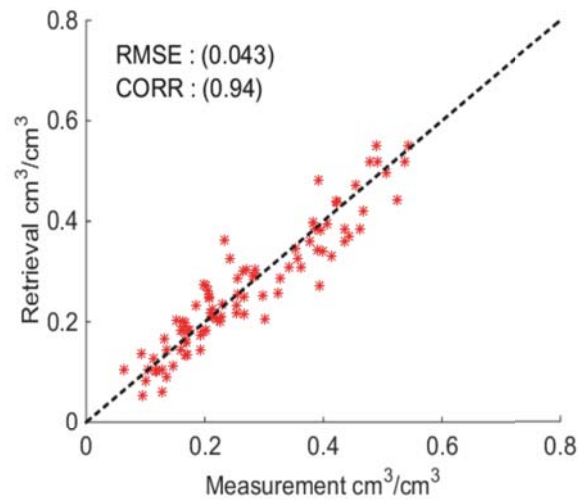


Figure 16. Retrieved soil moisture compared with measurements for the ten SMAPVEX12 wheat fields. The x and y axes represent the measured soil moisture and data-cube based retrieval results, respectively.

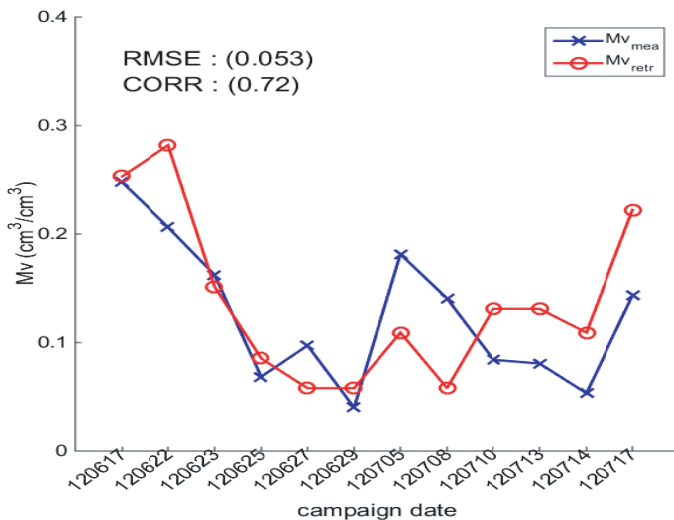


Figure 17. Time-series soil moisture retrieval for SMAPVEX12 canola Field 61.

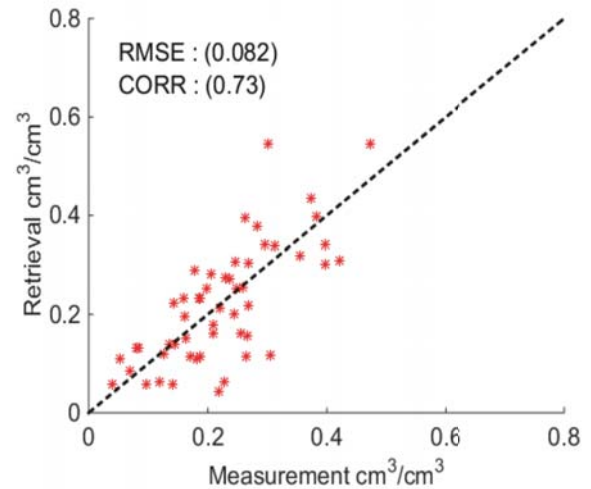


Figure 18. Retrieved soil moisture compared with measurements for the five SMAPVEX12 canola fields. The x and y axes represent the measured soil moisture and data-cube based retrieval results, respectively.

the empirical tuning was performed only on the vegetation parameterization over the entire field, not for individual fields. The retrieval error mainly originates from the radar measurements, data-cube modeling, and dielectric model, as discussed in more detail in [12]. Considering the uncertainties of in situ soil moisture measurement ($< 0.03 \text{ cm}^3/\text{cm}^3$ [37]), the actual error could be smaller. The retrieval error can be further reduced by updating the data-cubes with more measurement data. Generally, the retrieval soil moistures based on the data-cubes are in good agreement with ground measured soil moistures.

Table 15. RMSE and correlation coefficient of soil moisture between retrieval results and ground measurements for the five canola fields.

Field No.	RMSE (cm ³ /cm ³)	Correlation Coefficient
124	0.082	0.66
122	0.075	0.65
115	0.10	0.83
84	0.089	0.43
61	0.053	0.72

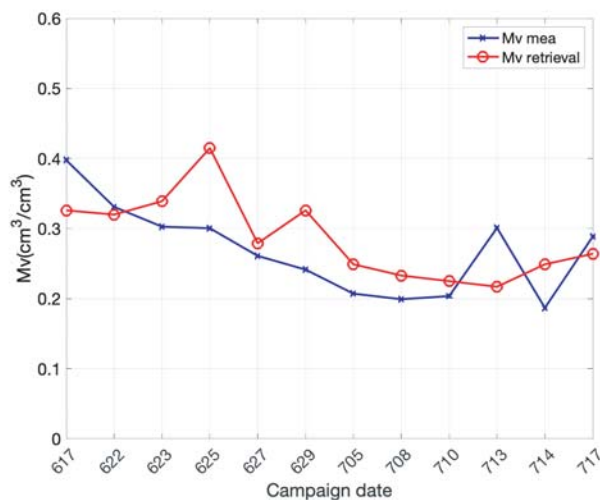


Figure 19. Time-series soil moisture retrieval for SMAPVEX12 pasture Field 21, RMSE = 0.06 (cm³/cm³), CORR = 0.54.

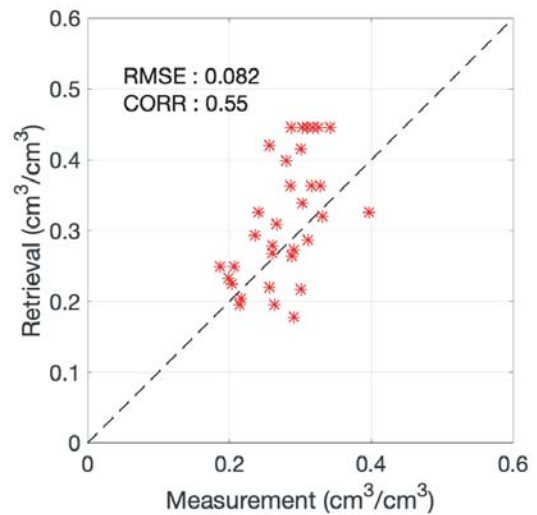


Figure 20. Retrieved soil moisture compared with measurements for the three SMAPVEX12 pasture fields. The x and y axes represent the measured soil moisture and data-cube based retrieval results, respectively.

Table 16. RMSE and correlation coefficient of soil moisture between retrieval results and ground measurements for the three pasture fields ($w_{VV} = 0.9$ and $w_{HH} = 0.1$).

Field No.	RMSE (cm ³ /cm ³)	Correlation Coefficient
21	0.059	0.54
22	0.055	0.63
23	0.122	0.68

7. CONCLUSIONS

Wheat, canola, and pasture data-cubes are developed based on physical scattering models to support radar retrieval of soil moisture for the SMAP and NISAR satellite missions. The physical model combines the distorted Born approximation with the NMM3D of rough surface scattering. The backscattering coefficients of the data-cubes are in good agreement with the UAVSAR data collected during the SMAPVEX12 field campaign over a wide range of VWC and soil moisture. Correlation coefficients are 0.84, 0.93, and 0.68 for HH, and 0.85, 0.77, and 0.82 for VV of wheat, canola, and pasture fields, respectively. The RMSEs are 0.82 dB, 0.78 dB, and 1.62 dB for HH, and 0.97 dB, 1.30 dB,

and 1.82 dB for VV of wheat, canola and pasture fields, respectively. The rms errors for the L-band backscattering coefficient from the data-cubes are generally smaller than that from the MIMICS model applied in [20].

The L-band time-series retrieval algorithm was implemented to retrieve the soil moisture using the data-cubes, resulting in an RMSE of $0.043 \text{ cm}^3/\text{cm}^3$ for the wheat fields, compared with the in-situ soil moisture from SMAPVEX12. The retrieval performance for the canola fields is not as good, an RMSE of $0.082 \text{ cm}^3/\text{cm}^3$, mainly because the volume scattering, which is independent of soil moisture, dominates among the backscattering mechanisms. The retrieval for the pasture fields has RMSE of $0.082 \text{ cm}^3/\text{cm}^3$. The volume scattering could contribute significantly which hinders the retrieval performance to certain degrees. It is shown that the retrieval results of the baseline active retrieval algorithms are in good agreement with in-situ soil moisture measurements, showing good performance of the retrieval algorithm.

The results in the paper provide the theoretical basis of the SMAP radar algorithm. These have been applied to the 3 months of SMAP radar data [15] and will be used in NISAR's global soil moisture retrieval. In the future, the data-cubes will be refined with more field campaign data sets so that the retrieval accuracy can be further improved, especially for the canola data-cubes. The results of distorted Born approximation and data cubes in this paper are benchmark results that can be used to compare and be calibrated against NMM3D full wave simulations of vegetated media.

ACKNOWLEDGMENT

The work in this paper was supported by the NASA SMAP project. The research described in this publication was carried out in part at the Jet Propulsion Laboratory, California Institute of Technology, under a contract with the National Aeronautics and Space Administration. We also thank the SMAPVEX12 field campaign team for providing the measurement data.

REFERENCES

1. Entekhabi, D., E. G. Njoku, P. E. O'Neill, K. H. Kellogg, W. T. Crow, W. N. Edelstein, et al., "The Soil Moisture Active Passive (SMAP) mission," *Proceedings of the IEEE*, Vol. 98, 704–716, May 2010.
2. Entekhabi, D., S. Yueh, P. O'Neill, and K. Kellogg, *SMAP Handbook*, 400–1567, JPL Publication JPL, 2014.
3. Tabatabaeejad, A., M. Burgin, and M. Moghaddam, "Potential of L-band radar for retrieval of canopy and subcanopy parameters of boreal forests," *IEEE Transactions on Geoscience and Remote Sensing*, Vol. 50, 2150–2160, Jun. 2012.
4. Kellogg, K., P. Hoffman, S. Standley, S. Shaffer, P. Rosen, W. Edelstein, et al., "NASA-ISRO Synthetic Aperture Radar (NISAR) mission," *2020 IEEE Aerospace Conference*, 2020.
5. Amelung, F., *NASA-ISRO SAR (NISAR) Mission Science Users' Handbook*, Jet Propulsion Laboratory (U.S.), 2019.
6. Stavros, N., P. Siqueira, M. Cosh, N. Torbick, and B. Osmanoglu, *2018 NISAR Applications Workshop: Agriculture and Soil Moisture*, 2018.
7. *NISAR: The NASA-ISRO SAR Mission: Vital for Life and Civilization*, available: https://nisar.jpl.nasa.gov/system/documents/files/15_NISARApplications_SoilMoisture1.pdf.
8. Kim, Y. and J. J. Van Zyl, "A time-series approach to estimate soil moisture using polarimetric radar data," *IEEE Transactions on Geoscience and Remote Sensing*, Vol. 47, 2519–2527, 2009.
9. Joseph, A. T., R. van der Velde, P. E. O'Neill, R. H. Lang, and T. Gish, "Soil moisture retrieval during a corn growth cycle using L-band (1.6 GHz) radar observations," *IEEE Transactions on Geoscience and Remote Sensing*, Vol. 46, 2365–2374, 2008.
10. De Roo, R. D., Y. Du, F. T. Ulaby, and M. C. Dobson, "A semi-empirical backscattering model at L-band and C-band for a soybean canopy with soil moisture inversion," *IEEE Transactions on Geoscience and Remote Sensing*, Vol. 39, 864–872, Apr. 2001.

11. Kim, S. B., L. Tsang, J. T. Johnson, S. Huang, J. J. van Zyl, and E. G. Njoku, "Soil moisture retrieval using time-series radar observations over bare surfaces," *IEEE Transactions on Geoscience and Remote Sensing*, Vol. 50, 1853–1863, May 2012.
12. Kim, S. B., M. Moghaddam, L. Tsang, M. Burgin, X. L. Xu, and E. G. Njoku, "Models of L-band radar backscattering coefficients over global terrain for soil moisture retrieval," *IEEE Transactions on Geoscience and Remote Sensing*, Vol. 52, 1381–1396, Feb. 2014.
13. Mironov, V. L., M. C. Dobson, V. H. Kaupp, S. A. Komarov, and V. N. Kleshchenko, "Generalized refractive mixing dielectric model for moist soils," *IEEE Transactions on Geoscience and Remote Sensing*, Vol. 42, 773–785, Apr. 2004.
14. Hallikainen, M. T., F. T. Ulaby, M. C. Dobson, M. A. Elrayes, and L. K. Wu, "Microwave dielectric behavior of wet soil. 1. Empirical-models and experimental-observations," *IEEE Transactions on Geoscience and Remote Sensing*, Vol. 23, 25–34, 1985.
15. Kim, S.-B., J. J. Van Zyl, J. T. Johnson, M. Moghaddam, L. Tsang, A. Colliander, et al., "Surface soil moisture retrieval using the L-band synthetic aperture radar onboard the Soil Moisture Active-Passive satellite and evaluation at core validation sites," *IEEE Transactions on Geoscience and Remote Sensing*, Vol. 55, 1897–1914, 2017.
16. Huang, H., S.-B. Kim, L. Tsang, X. Xu, T.-H. Liao, T. J. Jackson, et al., "Coherent model of L-band radar scattering by soybean plants: Model development, evaluation, and retrieval," *IEEE Journal of Selected Topics in Applied Earth Observations and Remote Sensing*, Vol. 9, 272–284, 2016.
17. Liao, T. H., S. B. Kim, S. R. Tan, L. Tsang, C. X. Su, and T. J. Jackson, "Multiple scattering effects with cyclical correction in active remote sensing of vegetated surface using vector radiative transfer theory," *IEEE Journal of Selected Topics in Applied Earth Observations and Remote Sensing*, Vol. 9, 1414–1429, Apr. 2016.
18. Lang, R. H. and J. S. Sidhu, "Electromagnetic backscattering from a layer of vegetation — A discrete approach," *IEEE Transactions on Geoscience and Remote Sensing*, Vol. 21, 62–71, 1983.
19. Tsang, L., J. A. Kong, and R. T. Shin, *Theory of Microwave Remote Sensing*, Wiley, New York, 1985.
20. Toure, A., K. P. B. Thomson, G. Edwards, R. J. Brown, and B. G. Brisco, "Adaptation of the mimics backscattering model to the agricultural context — Wheat and canola at L and C bands," *IEEE Transactions on Geoscience and Remote Sensing*, Vol. 32, 47–61, Jan. 1994.
21. Ulaby, F. T., K. Sarabandi, K. McDonald, M. Whitt, and M. C. Dobson, "Michigan microwave canopy scattering model," *International Journal of Remote Sensing*, Vol. 11, 1223–1253, Jul. 1990.
22. Tsang, L. and J. A. Kong, *Scattering of Electromagnetic Waves, Advanced Topics*, Vol. 26, John Wiley & Sons, 2004.
23. Huang, H., T.-H. Liao, L. Tsang, E. G. Njoku, A. Colliander, T. J. Jackson, et al., "Modelling and validation of combined active and passive microwave remote sensing of agricultural vegetation at L-band," *Progress In Electromagnetics Research B*, Vol. 78, 91–124, 2017.
24. Lang, R. H. and N. Khadr, "Effects of backscattering enhancement on soil-moisture sensitivity," *International Space Year: Space Remote Sensing, Vols. 1 and 2*, 916–919, 1992.
25. Huang, S. and L. Tsang, "Electromagnetic scattering of randomly rough soil surfaces based on numerical solutions of Maxwell equations in three-dimensional simulations using a hybrid UV/PBTG/SMCG method," *IEEE Transactions on Geoscience and Remote Sensing*, Vol. 50, 4025–4035, 2012.
26. McNairn, H., T. J. Jackson, G. Wiseman, S. Belair, A. Berg, P. Bullock, et al., "The Soil Moisture Active Passive Validation Experiment 2012 (SMAPVEX12): Prelaunch calibration and validation of the SMAP soil moisture algorithms," *IEEE Transactions on Geoscience and Remote Sensing*, Vol. 53, 2784–2801, 2015.
27. Huang, H., L. Tsang, E. G. Njoku, A. Colliander, T.-H. Liao, and K.-H. Ding, "Propagation and scattering by a layer of randomly distributed dielectric cylinders using Monte Carlo simulations of 3D Maxwell equations with applications in microwave interactions with vegetation," *IEEE Access*, Vol. 5, 11985–12003, 2017.

28. Huang, H., L. Tsang, A. Colliander, and S. H. Yueh, "Propagation of waves in randomly distributed cylinders using three-dimensional vector cylindrical wave expansions in Foldy-Lax equations," *IEEE Journal on Multiscale and Multiphysics Computational Techniques*, Vol. 4, 214–226, 2019.
29. Gu, W. and L. Tsang, "Vegetation effects for remote sensing of soil moisture using NMM3D full-wave simulation," *IEEE Antennas and Propagation Symposium*, Montreal, 2020.
30. Huang, H., T.-H. Liao, L. Tsang, E. G. Njoku, A. Colliander, T. J. Jackson, et al., "Modelling and validation of combined active and passive microwave remote sensing of agricultural vegetation at L-band," *Progress In Electromagnetics Research*, Vol. 78, 91–124, 2017.
31. Ulaby, F. T., D. G. Long, W. J. Blackwell, C. Elachi, A. K. Fung, C. Ruf, et al., *Microwave Radar and Radiometric Remote Sensing*, 2014.
32. Tsang, L., J. Kong, and K.-H. Ding, *Scattering of Electromagnetic Waves: Theories and Applications*, John Wiley & Sons, ed: Inc, 2000.
33. Hensley, S., K. Wheeler, G. Sadowy, C. Jones, S. Shaffer, H. Zebker, et al., "The UAVSAR instrument: Description and first results," *2008 IEEE Radar Conference, Vols. 1–4*, 827–832, 2008.
34. Mladenova, I. E., T. J. Jackson, R. Bindlish, and S. Hensley, "Incidence angle normalization of radar backscatter data," *IEEE Transactions on Geoscience and Remote Sensing*, Vol. 51, 1791–1804, Mar. 2013.
35. Deng, H., G. Farquharson, J. Sahr, Y. Goncharenko, and J. Mower, "Phase calibration of an along-track interferometric FMCW SAR," *IEEE Transactions on Geoscience and Remote Sensing*, Vol. 56, 4876–4886, 2018.
36. Rowlandson, T. L., A. A. Berg, P. R. Bullock, E. R. Ojo, H. McNairn, G. Wiseman, et al., "Evaluation of several calibration procedures for a portable soil moisture sensor," *Journal of Hydrology*, Vol. 498, 335–344, Aug. 19, 2013.
37. Cosh, M. H., T. J. Jackson, R. Bindlish, J. S. Famiglietti, and D. Ryu, "Calibration of an impedance probe for estimation of surface soil water content over large regions," *Journal of Hydrology*, Vol. 311, 49–58, Sep. 15, 2005.
38. Ulaby, F. T. and M. A. Elrayes, "Microwave dielectric spectrum of vegetation. 2. Dual-dispersion model," *IEEE Transactions on Geoscience and Remote Sensing*, Vol. 25, 550–557, Sep. 1987.